Label-Efficient Hyperspectral Image Classification via Spectral FiLM Modulation of Low-Level Pretrained Diffusion Features

Yuzhen Hu* YHU33@COUGARNET.UH.EDU
University of Houston, Texas, USA

Biplab Banerjee BBANERJEE@IITB.AC.IN
Indian Institute of Technology Bombay, India

Saurabh Prasad* SAURABH.PRASAD@IEEE.ORG
University of Houston, Texas, USA

Abstract

Hyperspectral imaging (HSI) enables detailed land cover classification, but low spatial resolution and sparse annotations pose significant challenges. We present a label-efficient framework that leverages spatial features from a frozen diffusion model pretrained on natural images. Specifically, we extract low-level representations from high-resolution decoder layers at early denoising timesteps, which transfer well to the low-texture setting of HSI. To combine spectral and spatial information, we introduce a lightweight FiLM-based fusion module that adaptively integrates spectral cues into frozen spatial features, enabling effective multimodal learning under sparse supervision. Experiments on two recent hyperspectral datasets show that our method outperforms state-of-the-art approaches using only the sparse training labels provided. Ablation studies further validate the benefit of diffusion-based features and spectral-aware fusion. Our results suggest that pretrained diffusion models can support domain-agnostic, label-efficient representation learning in remote sensing and scientific imaging tasks.

Keywords: Diffusion Models, Hyperspectral Imaging, Remote Sensing, Label-Efficient Learning, Land Cover Mapping

1. Introduction

Land cover mapping is a fundamental task in remote sensing, supporting applications such as environmental monitoring, agriculture, and resource management. Hyperspectral images (HSIs), with their dense spectral reflectance information, provide detailed insights into material properties and are well-suited for this purpose.

Despite their rich spectral content, HSIs pose several challenges. Their high dimensionality increases computational cost and overfitting risk, especially under limited supervision. Moreover, the trade-off between spectral fidelity and spatial resolution often leads to poor spatial detail, limiting segmentation accuracy.

Additional challenges arise from the spectral and spatial variability of land cover types across regions. Subtle intra-class variations—due to differences in vegetation, soil, or human activity—make generalization difficult Akiva et al. (2022); Liu et al. (2024); Prasad et al. (2024); Kumar et al. (2023);

* Co-corresponding author

Li et al. (2023). Finally, acquiring high-quality labeled data is expensive and time-consuming, as pixel-level annotation requires domain expertise. These limitations highlight the need for approaches that can extract robust features without heavy reliance on labels. Unsupervised and self-supervised learning methods address this by learning directly from the data.

Generative models—particularly diffusion models Ho et al. (2020); Song et al. (2020); Sohl-Dickstein et al. (2015); Dhariwal and Nichol (2021); Pang et al. (2024)—have recently shown state-of-the-art performance in image synthesis, restoration, and manipulation tasks. Through unsupervised training and iterative denoising, diffusion models learn the underlying data distribution, enabling them to capture rich spatial structures and pixel-wise contextual dependencies—traits especially valuable for segmentation and representation learning under data scarcity.

Unlike deterministic self-supervised methods such as masked autoencoders He et al. (2022), diffusion models operate in a probabilistic framework that better handles uncertainty and degraded inputs. This makes them well-suited for low-resolution, low-texture hyperspectral imagery Chen et al. (2020); Zhang et al. (2023a). Notably, Baranchuk et al. (2021) demonstrated that pre-trained diffusion models can provide strong pixel-level representations, outperforming earlier self-supervised methods under limited supervision and maintaining robustness under corrupted inputs. Pre-trained diffusion models have shown impressive performance in natural image domains Xu et al. (2023); Zhang et al. (2023a), yet their application to geospatial imagery remains underexplored. This is due in part to significant domain shifts—differences in spatial scale, viewing geometry, and spectral coverage (e.g., near and short-wave infrared)—which challenge cross-domain generalization Wang et al. (2021); Zhang et al. (2023b).

Beyond domain shift, hyperspectral imagery introduces a unique modality challenge: each pixel contains a high-dimensional spectral signature critical for land cover analysis. Effectively leveraging both spectral and spatial information—especially under limited supervision—requires models capable of adaptive fusion conditioned on spectral features. To address this, we adopt FiLM-based modulation Perez et al. (2018) , a lightweight and parameter-efficient conditioning method that remains largely unexplored in hyperspectral settings.

This work addresses two key challenges in hyperspectral land cover mapping: (1) transferring pre-trained diffusion models to geospatial domains, and (2) enabling adaptive fusion of spatial and spectral modalities under sparse supervision. We introduce **GeoDiffNet-F**, a label-efficient framework that reuses a diffusion model pre-trained on natural images to extract transferable spatial features, which are fused with spectral embeddings using FiLM-based modulation. Our contributions are as follows:
(1) We propose **GeoDiffNet**, a lightweight framework that repurposes frozen decoder layers of pre-trained diffusion models to extract low-level spatial features that generalize well to geospatial imagery with weak texture and low resolution;
(2) we demonstrate strong cross-domain transferability of diffusion features without requiring domain-specific finetuning;
(3) we introduce **GeoDiffNet-F**, which fuses spectral and spatial features using FiLM-based modulation, enabling dynamic, feature-wise conditioning from spectral input;
(4) we perform a detailed transferability analysis across decoder layers and denoising

timesteps, showing that early diffusion features are robust to significant domain shift.

2. Related work

Feature Transferability in Deep Learning has been extensively studied, particularly with convolutional neural networks (CNNs). Early layers in CNNs capture low-level features, such as edges and textures, which are highly transferable across different tasks and datasets Yosinski et al. (2014); Long et al. (2016). This principle has been foundational in the success of transfer learning, enabling models pre-trained on large-scale datasets to be fine-tuned for specific tasks with smaller datasets.

Diffusion Models as a new class of generative models, have shown remarkable performance in generating high-fidelity images. These models learn to generate data by reversing a diffusion process, progressively transforming noise into structured data. Recent advancements Ho et al. (2020); Song et al. (2020); Dhariwal and Nichol (2021) have positioned diffusion models as state-of-the-art in image generation tasks.

Diffusion Models for Feature Extraction. The potential of diffusion models for feature extraction has attracted growing interest. Prior studies Baranchuk et al. (2021); Xu et al. (2023); Zhang et al. (2023a); Luo et al. (2023) extract features from various layers of the U-Net architecture and timesteps in the diffusion process, leveraging multi-scale and multi-timestep information for robust pixel-level descriptors in tasks like image segmentation. However, these works assume a well-aligned source and target domain. To date, no studies have investigated the use of diffusion-based features in cross-domain settings, leaving their generalizability underexplored.

Diffusion Models in Remote Sensing. Diffusion models have recently gained attention in remote sensing Bandara et al. (2022); Ayala et al. (2023); Bai et al. (2022); Chen et al. (2023); Pang et al. (2024). Most prior work trains models from scratch or tailors them to specific datasets—e.g., Chen et al. (2023) proposes a 3D diffusion model for hyperspectral data that demands substantial computation and large training sets. In contrast, we are the first to evaluate a universal pre-trained diffusion model for geospatial analysis, assessing its feature transferability to hyperspectral imagery without additional training.

Hyperspectral Images (HSI) Land-Cover Mapping. Hyperspectral imagery (HSI) enables fine-grained land-cover classification by capturing rich spectral information across hundreds of contiguous bands Prasad et al. (2014); Wu and Prasad (2016); Li et al. (2012). Recent methods adopt multimodal fusion (e.g., HSI with RGB or SAR) Wang et al. (2022) and transformer-based architectures Hong et al. (2021a), but rely heavily on full supervision, where performance depends on the availability of labeled data. In contrast, we are the first to leverage a universal pre-trained diffusion model for HSI land-cover mapping, extracting strong transferable features without task-specific training and significantly reducing label requirements.

3. Proposed Methodology

3.1. Overview of GeoDiffNet and GeoDiffNet-F

Our framework consists of two complementary branches, as illustrated in Figure 1. The **GeoDiffNet** branch focuses on spatial feature extraction by leveraging a frozen diffusion model pretrained on natural RGB images. Specifically, we extract per-pixel features from low-level decoder layers at low denoising timesteps (e.g., T=0, 50, 100), which are shown to capture meaningful local struc-

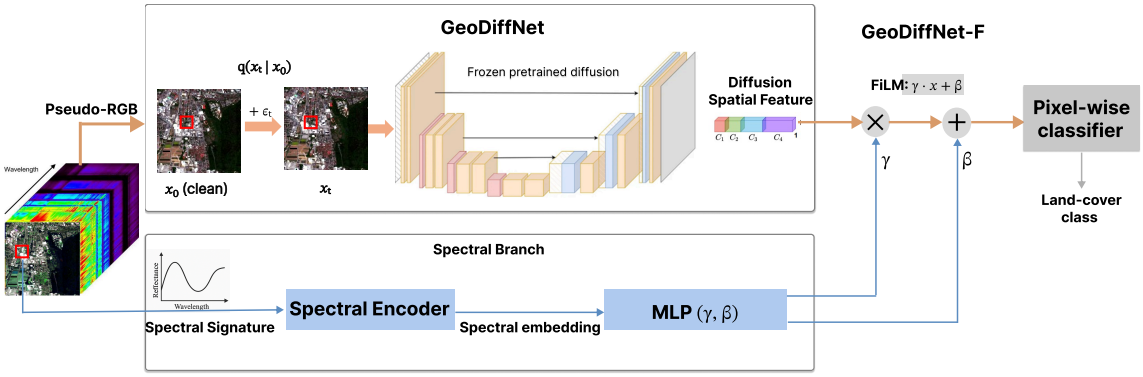

Figure 1: **Workflow of GeoDiffNet and GeoDiffNet-F.** GeoDiffNet extracts low-level spatial features from RGB-like patches using a frozen pretrained diffusion model. A lightweight MLP is applied to each pixel for classification. GeoDiffNet-F further incorporates spectral context by encoding per-pixel reflectance signals into spectral embeddings, which are used to regress scaling (γ) and shifting (β) vectors through an MLP. These vectors condition the spatial features via a FiLM layer, enabling adaptive cross-modal fusion for land-cover classification.

ture even under resolution constraints. Each hyperspectral image is divided into overlapping pseudo-RGB patches (e.g., 64×64 with stride 32), and the extracted features are passed through a lightweight MLP for adaptation.

In parallel, the **spectral branch** encodes each pixel's full spectral signature using a dedicated spectral encoder, followed by an MLP that predicts FiLM parameters (scaling γ and shifting β). These modulation parameters are used to condition the spatial features through a FiLM layer, enabling dynamic feature adaptation across modalities.

Finally, the **GeoDiffNet-F** module performs adaptive multimodal fusion. The modulated spatial features are passed to a 2-layer MLP for final pixel-wise land-cover classification. This design allows the model to benefit from both local spatial cues captured by the diffusion model and detailed spectral information unique to hyperspectral imagery.

3.2. Diffusion Model for Spatial Feature Extraction

To extract spatial features from hyperspectral images (HSI), we first select three spectral bands corresponding to the red, green, and blue wavelengths to construct a pseudo-RGB image. We then employ a pretrained diffusion model (trained on ImageNet) Dhariwal and Nichol (2021); Nichol et al. (2021); Ranftl et al. (2021). This model is based on a U-Net architecture, consisting of an encoder and a decoder. The decoder integrates information from the encoder through skip connections and contains 12 layers with varying resolutions and channel sizes, including attention mechanisms at specific scales to capture both local and global dependencies. We choose a 64×64 input resolution to align with the patch-based nature of land-cover mapping, where large images are divided into small patches for dense classification. This resolution not only reduces computational cost, but also matches the training scale of the diffusion model, which is optimized to reconstruct local spatial structures—making it particularly

effective in low-texture or homogeneous regions common in HSI data. Additional implementation details about the pre-trained diffusion model are provided in Appendix D.

A diffusion model involves two process: inversion (forward) and reversion (generation). At $t = 0$, we extract the feature representation of the clean image x_0. Using the forward process, we can directly compute the noisy image x_t at timestep t as follows:

$$x_t = \sqrt{\bar{\alpha}_t} x_0 + \sqrt{1 - \bar{\alpha}_t}\epsilon, \quad \epsilon \sim \mathcal{N}(0, 1), \quad (1)$$

with the corresponding conditional distribution:

$$q(x_t|x_0) := \mathcal{N}(x_t; \sqrt{\bar{\alpha}_t} x_0, (1 - \bar{\alpha}_t)I). \quad (2)$$

Here, $\bar{\alpha}_t$ represents the cumulative noise schedule up to timestep t.

The forward process is used because the equation allows us to calculate x_t and its distribution $q(x_t|x_0)$ from x_0 in a single step. This contrasts with the progressive generation process, which requires iterative computation of intermediate states, making the forward process more efficient for feature extraction in large-scale image processing.

Choosing the appropriate timestep t is crucial. Some studies suggest that early timesteps balance the original image and noise, providing richer feature representations Baranchuk et al. (2021). However, the optimal timestep is still under exploration. While $t = 0$ may retain original features best Xu et al. (2023), adding a bit of noise might enhance feature extraction Luo et al. (2023). We will first experiment with $t = 0$, 50, and 100 in Section 4.3 and then conduct an ablation study to evaluate its efficacy on transferability of different timestep in Section 4.5.

3.3. Pre-trained Diffusion Model for Geospatial Imagery

Given that geospatial images exhibit significant disparities from the natural images typically used to pre-train diffusion models, a key question arises: can these pre-trained diffusion models effectively extract the spatial features needed from geospatial imagery?

Low-Level Features: These are captured by the initial layers of the network and typically include basic patterns such as edges, textures, and simple shapes. In the context of the U-Net decoder, this would correspond to a layer close to the output (e.g. layer 9-11, with layer numbered from bottom to up).

High-Level Features: These are captured by the deeper layers of the network and involve more complex and abstract representations, such as parts of objects or entire objects. In the context of the U-Net decoder,this would generally correspond to decoder layers closer to the bottom of the UNet (e.g., layers 2-5)

According to Long et al. (2015), deep models' lower-level features have high transferability in domain adaptation. In the diffusion model U-Net architecture context, it's reasonable to conclude that the diffusion model's U-Net decoder, with its upper side (layer 9-11) corresponding to low-level features, can still effectively capture spatial features for geospatial image analysis tasks, despite the significant domain discrepancy.

3.4. Efficacy of Low-Level Features

Our goal is to evaluate the transferability of features extracted from a pre-trained diffusion model in the context of hyperspectral land-cover mapping. Specifically, we investigate whether spatial features obtained from shallow decoder layers and low-noise timesteps generalize better across domains.

Features extracted from a pre-trained diffusion model exhibit a dual hierarchy formed by both the model architecture and the denoising process. The spatial hierarchy is reflected across U-Net decoder layers: deeper layers encode high-level semantic features

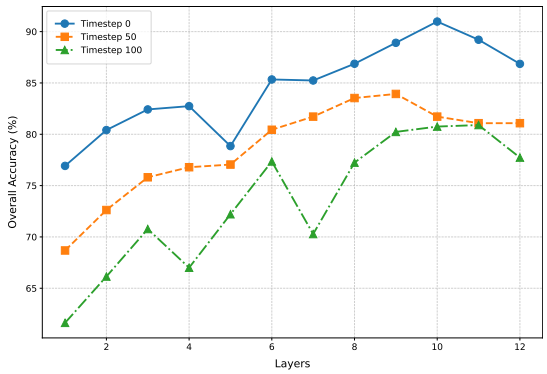

(a) Augsburg

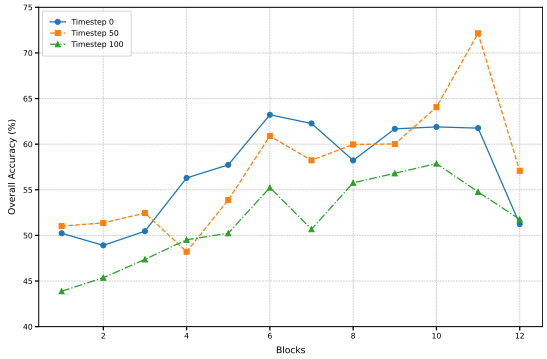

(b) Berlin

Figure 2: Both dataset performance metrics peak at **higher layers**, capturing **low-level features**. (a) **Augsburg**: performance peaks at layer 10 (timestep 0). (b) **Berlin**: performance peaks at layer 11 (timestep 50).

aligned with the pre-training domain, while shallower layers retain low-level spatial detail that is often more general and transferable. The temporal hierarchy arises across denoising timesteps: features at high-noise timesteps capture coarse, global structure, whereas those at low-noise timesteps recover finer, local details. Given the domain discrepancy between natural images used for pre-training and the target geospatial imagery, we hypothesize that low-level features (extracted from shallow decoder layers and low-noise timesteps) remain effective and transferable, as visualized in Appendix A.

To examine spatial transferability, we extract pixel-level features from decoder layers 2 to 11, where lower layers (2–5) are known to encode high-level abstractions and upper layers (9–11) retain low-level spatial patterns. These features are obtained from pseudo-RGB input patches (64×64, stride 32), passed through the frozen diffusion model. A lightweight two-layer MLP is applied to classify each pixel based on the extracted feature vector.

This setup enables a systematic evaluation of feature transferability across both spatial and temporal axes of the diffusion model. We use overall accuracy (OA), average accuracy (AA), and kappa coefficient (KC) to assess which layer–timestep combinations yield the most transferable features. Full results and analysis are presented in Section 4.5.

3.5. Spectrally-Conditioned Spatial Modulation

We propose a spectrally-conditioned spatial modulation mechanism using *Feature-wise Linear Modulation (FiLM)* to adapt spatial features based on per-pixel spectral input. A frozen pretrained diffusion model is used to extract spatial feature vectors $f_i^{\text{spatial}} \in \mathbb{R}^d$ from pseudo-RGB image patches. These spatial features capture structural and contextual patterns but lack detailed spectral information.

To incorporate spectral context, each pixel's hyperspectral signature $s_i \in \mathbb{R}^b$, where b denotes the number of spectral bands, is passed through a lightweight spectral encoder to produce a compact embedding. This embedding is then processed by a separate MLP to regress the FiLM modulation parameters: a scaling vector $\gamma(s_i) \in \mathbb{R}^d$ and a shifting vector $\beta(s_i) \in \mathbb{R}^d$. These parameters are applied to the corresponding spatial feature vector as follows:

$$\hat{f}_i = \gamma(s_i) \cdot f_i^{\text{spatial}} + \beta(s_i). \tag{3}$$

This pixel-wise conditioning enables the model to dynamically adapt spatial representations using the spectral characteristics of each pixel. Compared to traditional fusion methods such as concatenation or summation, FiLM allows for more flexible and learnable cross-modal interaction, leading to improved performance in land-cover classification tasks under limited supervision. An overview of this fusion strategy is illustrated in Figure 1.

GeoDiffNet-F: Extending Diffusion Features with Spectral Reflectance Information. Building on the spectrally-conditioned spatial modulation framework described above, we define GeoDiffNet-F as our final architecture for pixel-wise land-cover classification. Each pixel's hyperspectral signature is first encoded through a shallow MLP network, followed by an MLP that regresses FiLM modulation parameters. These parameters adapt the spatial features extracted from a frozen diffusion model, enabling spectral-to-spatial conditioning. The modulated features are passed to a lightweight classifier for prediction. As shown in Figure 1, this formulation enhances spatial representations using spectral context, resulting in improved performance under domain shift and low-label regimes.

4. Experimental Setup and Results

4.1. Dataset

To validate the proposed method, we use two publicly available hyperspectral datasets,Augsburg and Berlin,capturing urban and rural regions in Germany Hong et al. (2021b).

The Augsburg dataset was collected using the HySpex sensor and contains 180 spectral bands covering wavelengths from 0.4–2.5 µm. It has a spatial resolution of 30 m GSD and an image size of 332 × 485 pixels.

Table 1: Training and testing samples for the **Augsburg** dataset.

Class	Train Count	Test Count
Forest	146	13,361
Residential Area	264	30,065
Industrial Area	21	3,830
Low Plants	248	26,609
Allotment	52	523
Commercial Area	7	1,638
Water	23	1,507
Total	**761**	**77,533**

Table 2: Training and testing samples for the **Berlin** dataset.

Class	Train Count	Test Count
Forest	443	54,511
Residential Area	423	268,219
Industrial Area	499	19,067
Low Plants	376	58,906
Soil	331	17,095
Allotment	280	13,025
Commercial Area	298	24,526
Water	170	6,502
Total	**2,820**	**461,851**

The Berlin dataset, synthesized from HyMap HSI data to resemble EnMAP spectral characteristics, contains 244 bands over the same spectral range, with a resolution of 30 m GSD and dimensions of 797 × 220 pixels.

We adopt the original train/test splits from Hong et al. (2021b), summarized in Table 1 and Table 2, to ensure consistency and enable direct comparison with prior work Wang et al. (2022).

4.2. Implementation Details

Pre-trained Diffusion Model. We use the pre-trained diffusion model from Dhariwal and Nichol (2021) with a 64 × 64 patch size. This choice leverages the pretrained back-

bone without introducing additional trainable parameters, while providing abundant spatial context—over 30× larger than the typical 11×11 HSI patches used in geospatial tasks Ahmad et al. (2020)—allowing the model to capture long-range dependencies more effectively.

To utilize a pre-trained diffusion model, two decisions must be made: selecting between the encoder or decoder, and choosing between the forward or reverse process. We opt for the decoder, as in the U-Net architecture, the decoder integrates feature maps from the encoder via skip connections Baranchuk et al. (2021). **Forward process** is opted for feature extraction because it operates in a single timestep, making it more efficient than the progressive reverse process while achieving comparable performance Zhong et al. (2024); Luo et al. (2023).

Data Preparation. To prepare pseudo-RGB inputs for GeoDiffNet, we selected three representative spectral bands —- bands 40, 30, and 15 for Berlin, and bands 21, 11, and 6 for Augsburg —-since they approximately correspond to red, green, and blue wavelengths in the visible spectrum. This choice facilitates intuitive visualization and aligns with the RGB distribution seen during diffusion model pretraining. Hyperspectral images were divided into overlapping 64×64 patches with a stride of 32. Padding was applied to preserve spatial coverage and minimize edge artifacts.

GeoDiffNet. Each 64×64 pseudo-RGB patch was processed using a frozen pre-trained diffusion model. Decoder activations from layers 2 to 11 were resized to patch resolution for pixel-level alignment. For each labeled pixel, the corresponding spatial feature was used to train a two-layer MLP classifier, enabling evaluation across different layers and timesteps.

Spectral Branch. Each labeled pixel's spectral reflectance vector (180 bands for Augsburg, 244 for Berlin) was passed through a shallow MLP encoder. The output was used to regress FiLM parameters—scaling (γ) and shifting (β)—for feature modulation.

GeoDiffNet-F. We applied FiLM modulation to the frozen spatial features using the spectral FiLM parameters. The modulated features were passed through a two-layer MLP for final pixel-wise classification. Only the spectral branch and classifier were trained; the diffusion model remained frozen.

Training and Inference GeoDiffNet was trained to evaluate the effectiveness of frozen diffusion features, while GeoDiffNet-F was trained by optimizing the spectral branch—including the encoder and FiLM parameter regressor—and the classification layers, while keeping the diffusion-based spatial backbone frozen. We used a learning rate of 0.003, batch size of 64, and trained for up to 10 epochs with early stopping if no validation improvement occurred within 1000 iterations.

During inference, large geospatial images were divided into 64×64 patches with a stride of 32, creating overlapping regions. Pixel-wise predictions in overlapping areas were aggregated using max-voting to ensure smooth and accurate classification.

4.3. Evaluating the Efficacy of Low-Level Features

Qualitatively, as demonstrated in Figure 3 and Figure 4, using low-level feature layers, such as layer 11 for Berlin and layer 10 for Augsburg, GeoDiffNet's segmentation results are highly effective.

Compared to the ground truth maps, using pre-trained diffusion model-extracted low-level features only, GeoDiffNet produces sharp and well-defined boundaries between

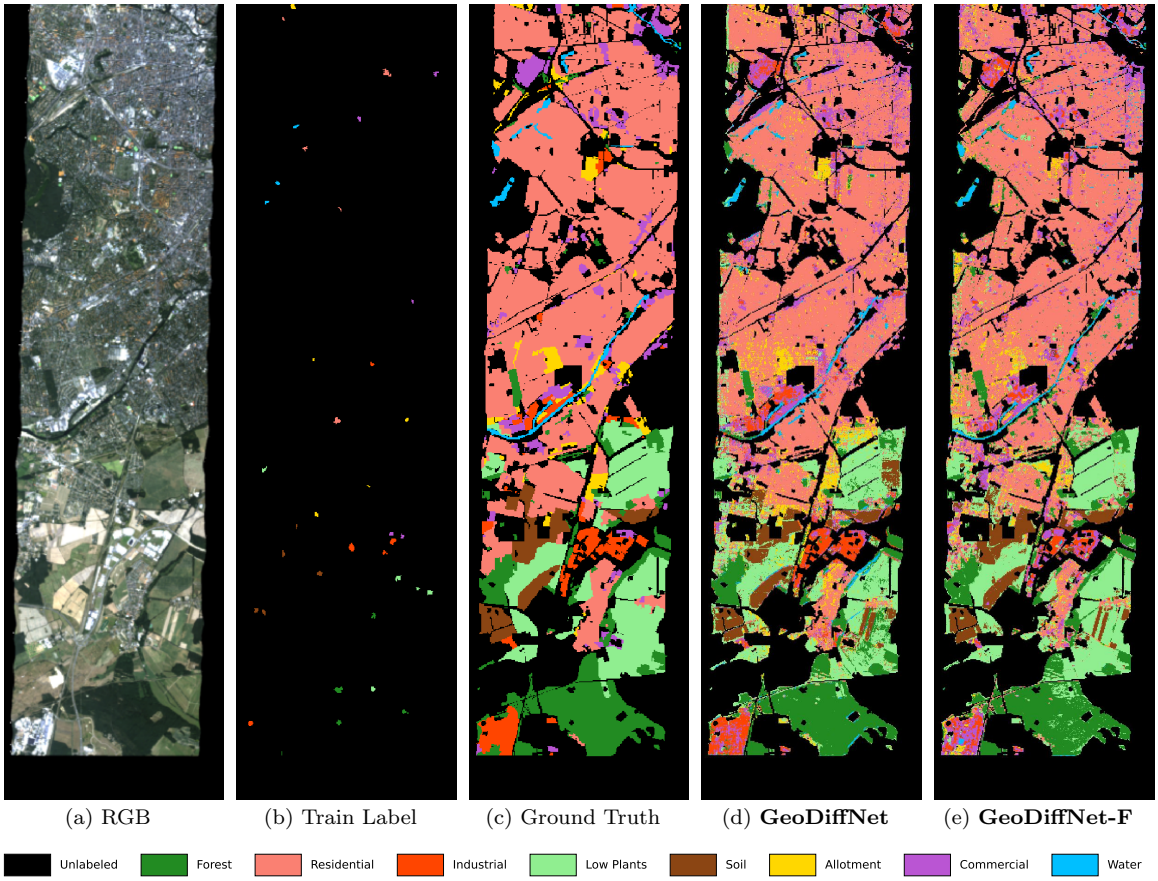

Figure 3: Visualization on **Berlin** HSI: (a) RGB image, (b) Training label map, (c) Ground truth, (d) **GeoDiffNet**, and (e) **GeoDiffNet-F**.

different land cover classes, accurately capturing intricate details. This highlights GeoDiffNet's capability to enhance spatial resolution and classification precision. More visualizations across different layers of comparison can be found in Appendix B.

Quantitively, from Table 4 and Table 3 , GeoDiffNet's low-level features, extracted using only HSI RGB 3 bands at higher layers, outperform several SOTA models that even rely on additional modalities in conjunction with HSI. For the Augsburg dataset, GeoDiffNet achieves an overall accuracy (OA) of 90.98% and an average accuracy (AA) of 65.05%, surpassing MIFNet and DFINet. For the Berlin dataset, GeoDiffNet records an OA of 72.15% and an AA of 60.74%, exceeding ContextCNN and comparable to DFINet.

Despite the significant disparity presented by geospatial imagery compared to the images that the pre-trained model has seen, as shown in GeoDiffNet's low-level features are highly effective. This proves our hypothesis that extracted low-level features have great transferability.

These results underscore the superior performance of GeoDiffNet's higher-layer low-level features, highlighting the model's ability to achieve high classification accuracy and distinguish between similar land cover classes only using a subset of available chan-

Table 3: Performance comparison on the **Berlin** dataset. TBCNN Xu et al. (2018), S2FL Hong et al. (2021b), ContextCNN Lee and Kwon (2017), DFINet Gao et al. (2021), and MIFNet Wang et al. (2022) are prior methods. **GeoDiffNet** uses spatial features from diffusion layer 11 of pseudo-RGB HSI; **GeoDiffNet-F** incorporates fused HSI spectral and spatial features.

Method	Modality	Forest	Res.	Indust.	L.Plants	Soil	Allot.	Comm.	Water	OA (%)	AA (%)	KC
TBCNN	HSI	71.52	60.80	69.58	68.57	80.39	97.55	35.25	82.77	63.85	69.55	0.3994
S2FL	HSI+SAR+DSM	83.30	57.39	48.53	77.16	83.84	57.05	31.02	61.57	62.23	62.48	0.4877
ContextCNN	HSI+SAR	77.22	63.69	61.44	73.77	87.22	82.88	31.13	74.24	66.31	68.95	0.5403
DFINet	HSI+SAR	68.95	67.52	43.42	81.77	75.58	80.05	40.94	79.87	67.93	67.26	0.5522
MIFNet	HSI+SAR	68.77	76.90	50.75	81.10	65.59	75.69	29.96	82.96	72.54	66.47	0.5981
GeoDiffNet	HSI	75.35	77.82	53.41	71.50	75.12	36.86	40.41	54.74	72.15	60.65	0.5850
GeoDiffNet-F	HSI	80.21	79.33	26.01	84.80	82.15	28.68	41.53	67.99	**74.44**	61.34	**0.6132**

Table 4: Performance comparison on the **Augsburg** dataset. TBCNN Xu et al. (2018), S2FL Hong et al. (2021b), ContextCNN Lee and Kwon (2017), DFINet Gao et al. (2021), and MIFNet Wang et al. (2022) are prior methods. **GeoDiffNet** uses spatial features from diffusion layer 10 of pseudo-RGB HSI; **GeoDiffNet-F** incorporates fused HSI spectral and spatial features.

Method	Modality	Forest	Res.	Indust.	L.Plants	Allot.	Comm.	Water	OA (%)	AA (%)	KC
TBCNN	HSI	94.71	96.37	69.30	81.58	62.52	12.70	16.39	86.12	61.94	0.8024
S2FL	HSI+SAR+DSM	88.80	86.36	38.90	90.53	68.64	8.97	47.45	83.36	61.38	0.7626
ContextCNN	HSI+SAR	94.57	97.25	51.46	86.25	56.02	13.68	21.57	87.24	60.11	0.8182
DFINet	HSI+SAR	95.38	95.84	69.79	86.65	64.05	13.86	28.47	88.06	64.86	0.8298
MIFNet	HSI+SAR	92.28	96.53	59.53	90.79	59.46	17.58	51.43	89.21	66.80	0.8453
GeoDiffNet	HSI	92.78	98.04	61.46	95.98	86.42	6.35	14.33	90.98	65.05	0.8682
GeoDiffNet-F	HSI	91.77	98.02	64.18	95.67	86.42	12.33	28.80	**91.23**	**68.17**	**0.8726**

nels in HSI, in contrast to other models that utilize the full spectrum and some that even require multiple modalities in addition to HSI.

4.4. Efficacy of GeoDiffNet-F

Qualitatively, as shown in Figure 4 and Figure 3, GeoDiffNet-F exhibits clear improvements over GeoDiffNet for both Augsburg and Berlin datasets.

Quantitatively, as shown in Table 4 and Table 3, GeoDiffNet-F with FiLM-based spectral fusion achieves the highest overall accuracy (OA) and Kappa coefficient (KC) on both datasets. Although its AA on Berlin is slightly lower than MIFNet, OA and KC provide a more balanced evaluation under class imbalance, highlighting the robustness of our method.

The strong performance of the GeoDiffNet-F fusion model is largely attributable to the spatial features extracted by GeoDiffNet. By effectively exploiting the spatial features inherent in HSI data, GeoDiffNet-F not only surpasses other SOTA fusion methods that depend on multiple data sources but also demonstrates the significant potential of GeoDiffNet-extracted spatial features in advancing hyperspectral image analysis.

4.5. Ablation Study: Timestep and Decoder Layer

To investigate critical design choices, we conducted a detailed ablation study on GeoDiffNet, focusing specifically on how timestep selection (noise levels) and decoder layer depth (spatial resolution) affect the quality

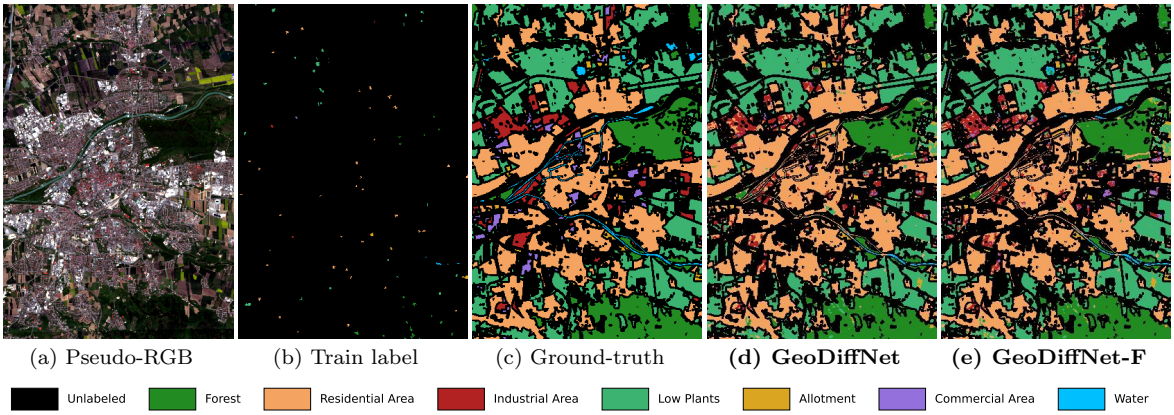

Figure 4: Visualization on **Augsburg** HSI: (a) Pseudo-RGB image, (b) Training label map, (c) Ground-truth, (d) **GeoDiffNet**, and (e) **GeoDiffNet-F**.

and transferability of extracted spatial features.

Impact of Timestep (Noise Level) Diffusion models introduce varying noise levels at different timesteps during the forward process. Lower timesteps correspond to cleaner images, whereas higher timesteps introduce progressively more noise. Our analysis as illustrated clearly in Appendix C indicates that early timesteps generally exhibit higher feature transferability due to proximity to the original data distribution, consistent with the *Chain of Forgetting theorem* Zhong et al. (2024).

However, our empirical findings highlight a nuanced observation: while clean images at timestep 0 yield optimal performance for Augsburg, a small amount of added noise at timestep 50 enhances feature extraction for Berlin. This aligns with previous studies Xu et al. (2023); Luo et al. (2023), which suggest that minimal noise can help retain critical spatial details, effectively balancing high-frequency information and smoothness for improved classification accuracy. Thus, while early timestep,low noise has more transferability, optimal timestep selection is not universally minimal and depends heavily on dataset-specific characteristics, reinforcing the necessity of carefully tuning this parameter.

Impact of Decoder Layer (Spatial Resolution) As diffusion models decode from lower to higher resolutions through progressive layers, deeper decoder layers yield more spatially detailed and accurate features. Our experiments demonstrate that higher layers consistently provide more informative representations, resulting in improved classification accuracy and better generalization to geospatial imagery. Specifically, optimal spatial feature extraction was achieved at **layer 10 for Augsburg** and **layer 11 for Berlin** (see detailed quantitative and qualitative analyses in Appendix B).

5. Conclusion

We demonstrate that pre-trained diffusion models can effectively transfer spatial representations to hyperspectral imagery without domain-specific fine-tuning. GeoDiffNet achieves strong pixel-level classification performance using only lightweight classifiers and minimal labeled data. By introducing FiLM-based spectral modulation, GeoDiffNet-F further improves performance through dynamic spatial–spectral fusion. Our analysis highlights that early de-

coder layers and lower noise timesteps yield the most transferable features, underscoring the potential of diffusion features as robust, label-efficient representations for remote sensing.

References

Muhammad Ahmad, Adil Mehmood Khan, Manuel Mazzara, Salvatore Distefano, Mohsin Ali, and Muhammad Shahzad Sarfraz. A fast and compact 3-d cnn for hyperspectral image classification. *IEEE Geoscience and Remote Sensing Letters*, 19: 1–5, 2020.

Peri Akiva, Matthew Purri, and Matthew Leotta. Self-supervised material and texture representation learning for remote sensing tasks. In *Proceedings of the IEEE/CVF Conference on Computer Vision and Pattern Recognition (CVPR)*, pages 8203–8215, June 2022.

C. Ayala, R. Sesma, C. Aranda, and M. Galar. Diffusion models for remote sensing imagery semantic segmentation. In *Proceedings of the Conference on Remote Sensing and Imaging*, Pamplona, Spain, 2023. Tracasa Instrumental, Institute of Smart Cities (ISC), Public University of Navarre. Email: {cayala, rsesma, caranda}@itracasa.es, mikel.galar@unavarra.es.

Wei Bai, Xinyu Zhang, Long Ma, Wei Hong, and Jian Yang. Conditional diffusion for sar to optical image translation. *Remote Sensing*, 14(10):2380, 2022.

Wele Gedara Chaminda Bandara, Nithin Gopalakrishnan Nair, and Vishal M Patel. Ddpm-cd: Denoising diffusion probabilistic models as feature extractors for change detection. *arXiv preprint arXiv:2206.11892*, 2022.

Dmitry Baranchuk, Ivan Rubachev, Andrey Voynov, Valentin Khrulkov, and Artem Babenko. Label-efficient semantic segmentation with diffusion models. *arXiv preprint arXiv:2112.03126*, 2021.

Mark Chen, Alec Radford, Rewon Child, Jeffrey Wu, Heewoo Jun, David Luan, and Ilya Sutskever. Generative pretraining from pixels. In *International conference on machine learning*, pages 1691–1703. PMLR, 2020.

Ning Chen, Jun Yue, Leyuan Fang, and Shaobo Xia. Spectraldiff: A generative framework for hyperspectral image classification with diffusion models. *IEEE Transactions on Geoscience and Remote Sensing*, 61:1–16, 2023.

Prafulla Dhariwal and Alexander Nichol. Diffusion models beat gans on image synthesis. *Advances in neural information processing systems*, 34:8780–8794, 2021.

Yunhao Gao, Wei Li, Mengmeng Zhang, Jianbu Wang, Weiwei Sun, Ran Tao, and Qian Du. Hyperspectral and multispectral classification for coastal wetland using depthwise feature interaction network. *IEEE Transactions on Geoscience and Remote Sensing*, 60:1–15, 2021.

Kaiming He, Xinlei Chen, Saining Xie, Yanghao Li, Piotr Dollár, and Ross Girshick. Masked autoencoders are scalable vision learners. In *Proceedings of the IEEE/CVF conference on computer vision and pattern recognition*, pages 16000–16009, 2022.

Jonathan Ho, Ajay Jain, and Pieter Abbeel. Denoising diffusion probabilistic models. *Advances in neural information processing systems*, 33:6840–6851, 2020.

Danfeng Hong, Zhu Han, Jing Yao, Lianru Gao, Bing Zhang, Antonio Plaza, and Jocelyn Chanussot. Spectralformer: Re-

thinking hyperspectral image classification with transformers. *IEEE Transactions on Geoscience and Remote Sensing*, 60:1–15, 2021a.

Danfeng Hong, Naoto Yokoya, Jocelyn Chanussot, and Xiao Xiang Zhu. Multimodal remote sensing benchmark datasets for land cover classification with a shared and specific feature learning model. *ISPRS Journal of Photogrammetry and Remote Sensing*, 178:137–150, 2021b.

Satish Kumar, Ivan Arevalo, ASM Iftekhar, and B S Manjunath. Methanemapper: Spectral absorption aware hyperspectral transformer for methane detection. In *Proceedings of the IEEE/CVF Conference on Computer Vision and Pattern Recognition (CVPR)*, pages 17609–17618, June 2023.

H. Lee and H. Kwon. Going deeper with contextual cnn for hyperspectral image classification. *IEEE Transactions on Image Processing*, 26(10):4843–4855, October 2017.

Miaoyu Li, Ji Liu, Ying Fu, Yulun Zhang, and Dejing Dou. Spectral enhanced rectangle transformer for hyperspectral image denoising. In *Proceedings of the IEEE/CVF Conference on Computer Vision and Pattern Recognition (CVPR)*, pages 5805–5814, June 2023.

Wei Li, Saurabh Prasad, James E Fowler, and Lori Mann Bruce. Locality-preserving discriminant analysis in kernel-induced feature spaces for hyperspectral image classification. *IEEE Journal of Selected Topics in Applied Earth Observations and Remote Sensing*, 5(1):153–166, 2012.

Sihan Liu, Yiwei Ma, Xiaoqing Zhang, Haowei Wang, Jiayi Ji, Xiaoshuai Sun, and Rongrong Ji. Rotated multi-scale interaction network for referring remote sensing image segmentation. In *Proceedings of the IEEE/CVF Conference on Computer Vision and Pattern Recognition*, pages 26658–26668, 2024.

Mingsheng Long, Yue Cao, Jianmin Wang, and Michael I Jordan. Learning transferable features with deep adaptation networks. *International conference on machine learning*, pages 97–105, 2015.

Mingsheng Long, Han Zhu, Jianmin Wang, and Michael I Jordan. Unsupervised domain adaptation with residual transfer networks. *Advances in neural information processing systems*, 29, 2016.

Grace Luo, Lisa Dunlap, Dong Huk Park, Aleksander Holynski, and Trevor Darrell. Diffusion hyperfeatures: Searching through time and space for semantic correspondence. *Advances in Neural Information Processing Systems*, 36:47500–47510, 2023.

Alexander Q Nichol, Prafulla Dhariwal, Aditya Ramesh, Pranav Shyam, Pamela Mishkin, Bob McGrew, Ilya Sutskever, and Mark Chen. Glide: Towards photorealistic image generation and editing with text-guided diffusion models. *arXiv preprint arXiv:2112.10741*, 2021.

Li Pang, Xiangyu Rui, Long Cui, Hongzhong Wang, Deyu Meng, and Xiangyong Cao. Hir-diff: Unsupervised hyperspectral image restoration via improved diffusion models. In *Proceedings of the IEEE/CVF Conference on Computer Vision and Pattern Recognition*, pages 3005–3014, 2024.

Ethan Perez, Florian Strub, Harm De Vries, Vincent Dumoulin, and Aaron Courville. Film: Visual reasoning with a general conditioning layer. In *Proceedings of the AAAI conference on artificial intelligence*, volume 32, 2018.

Saurabh Prasad, Ming Cui, Wei Li, and James E Fowler. Segmented mixture-of-gaussian classification for hyperspectral image analysis. *IEEE Geoscience and Remote Sensing Letters*, 11(1):138–142, 2014.

Saurabh Prasad, Jocelyn Chanussot, and Jun Li. *Advances in Machine Learning and Image Analysis for GeoAI*. Elsevier, Amsterdam, 2024. ISBN 9780443190773.

René Ranftl, Alexey Bochkovskiy, and Vladlen Koltun. Vision transformers for dense prediction. In *Proceedings of the IEEE/CVF international conference on computer vision*, pages 12179–12188, 2021.

Jascha Sohl-Dickstein, Eric Weiss, Niru Maheswaranathan, and Surya Ganguli. Deep unsupervised learning using nonequilibrium thermodynamics. In *International conference on machine learning*, pages 2256–2265. PMLR, 2015.

Yang Song, Jascha Sohl-Dickstein, Durk P Kingma, Abhishek Kumar, Stefano Ermon, and Ben Poole. Score-based generative modeling through stochastic differential equations. *arXiv preprint arXiv:2011.13456*, 2020.

Junjie Wang, Wei Li, Yunhao Gao, Mengmeng Zhang, Ran Tao, and Qian Du. Hyperspectral and sar image classification via multiscale interactive fusion network. *IEEE Transactions on Neural Networks and Learning Systems*, 34(12): 10823–10837, 2022.

Ting-Chun Wang, Ming-Yu Liu, and Jun-Yan Zhu. Pretraining is all you need for image-to-image translation. *arXiv preprint arXiv:2108.05930*, 2021.

Hao Wu and Saurabh Prasad. Dirichlet process based active learning and discovery of unknown classes for hyperspectral image classification. *IEEE Transactions on Geoscience and Remote Sensing*, 54(8):4882–4895, 2016.

Jiarui Xu, Sifei Liu, Arash Vahdat, Wonmin Byeon, Xiaolong Wang, and Shalini De Mello. Open-vocabulary panoptic segmentation with text-to-image diffusion models. In *Proceedings of the IEEE/CVF Conference on Computer Vision and Pattern Recognition*, pages 2955–2966, 2023.

Xiaodong Xu, Wei Li, Qiangqiang Ran, Qian Du, Liang Gao, and Bing Zhang. Multisource remote sensing data classification based on convolutional neural network. *IEEE Transactions on Geoscience and Remote Sensing*, 56(2):937–949, 2018.

Jason Yosinski, Jeff Clune, Yoshua Bengio, and Hod Lipson. How transferable are features in deep neural networks? *Advances in neural information processing systems*, 27, 2014.

Junyi Zhang, Charles Herrmann, Junhwa Hur, Luisa Polania Cabrera, Varun Jampani, Deqing Sun, and Ming-Hsuan Yang. A tale of two features: Stable diffusion complements dino for zero-shot semantic correspondence. *Advances in Neural Information Processing Systems*, 36:45533–45547, 2023a.

Lvmin Zhang, Anyi Rao, and Maneesh Agrawala. Adding conditional control to text-to-image diffusion models. In *Proceedings of the IEEE/CVF International Conference on Computer Vision (ICCV)*, pages 3836–3847, 2023b.

Jincheng Zhong, Xingzhuo Guo, Jiaxiang Dong, and Mingsheng Long. Diffusion tuning: Transferring diffusion models via chain of forgetting. *Advances in Neural Information Processing Systems*, 37:114574–114600, 2024.

Appendix

In Appendix A, we provide visualizations of the spatial features extracted by the diffusion model.

In Appendix B, We provide a detailed analysis of model performance over different layers of the diffusion model.

In Appendix C, we provide an analysis of model performance as a function of different timesteps in the diffusion model.

In Appendix D, we summarize the pretrained model used for feature extraction, detailing the resolution, channels, and attention at each decoder layer.

Code Availability. Our code is publicly available at https://github.com/hutuhehe/diffusion_hyperspectral.

Appendix A. Diffusion Spatial Feature Visualization

We present k-means clustering results ($k = 6$) on decoder features extracted from Layers 6–11 of a pretrained diffusion model, across timesteps from $T = 0$ to $T = 200$. Clustering is performed on a 64×64 pseudo-RGB patch sampled from the Berlin hyperspectral dataset, centered on the Messe Berlin convention center. Due to the low spatial resolution and limited texture in the input, object boundaries are not clearly visible. For reference, we include a high-resolution satellite image from Google Earth (circa 2009) to provide context on the actual scene layout.

Despite the degraded input quality, the diffusion-derived features produce semantically coherent clusters. Lower and intermediate decoder layers (e.g., Layers 6–7) tend to segment broad, coarse regions, while higher layers (e.g., Layers 9–11) better delineate object boundaries and suppress noise. This progression illustrates a shift from high-level abstraction in earlier layers to more detailed, spatially localized information in later layers.

Appendix B. Detailed Analysis for Dataset Augsburg and Berlin Over Layers

B.1. Augsburg Dataset

B.1.1. Visualization

In this experiment, we extract spatial features using the diffusion model at different layers and a fixed time-step 0, and evaluate layer informativeness based on performance. As shown in Figure 6, the figure illustrates the test labels and the inference (prediction) from the key informative layers (Layers 2, 5, 8, and 10) from the GeoDiffNet model for the Augsburg dataset. By comparing across different layers, we observe that as the layers progress higher, they become more informative. The progression through the layers demonstrates an increasing level of detail and accuracy in feature capture. Specifically, higher layers (Layer 10) exhibit more refined and precise feature representations, resulting in clearer delineations and more accurate classifications compared to the coarser and less detailed representations in the lower layers.

B.1.2. Performance as a function of diffusion model layers at time-steps 0, 50 and 100

Quantitatively, as shown in Table 5, Table 6 and Table 7, the analysis of U-Net layer performance in the diffusion model for the Augsburg dataset across timesteps 0, 50, and 100 demonstrates a clear trend: both overall and per-class performance metrics improve for higher layers, peaking around Layer 10/layer 11. Per class metrics all show significant gains at higher layers, indicating enhanced classification precision and agreement.

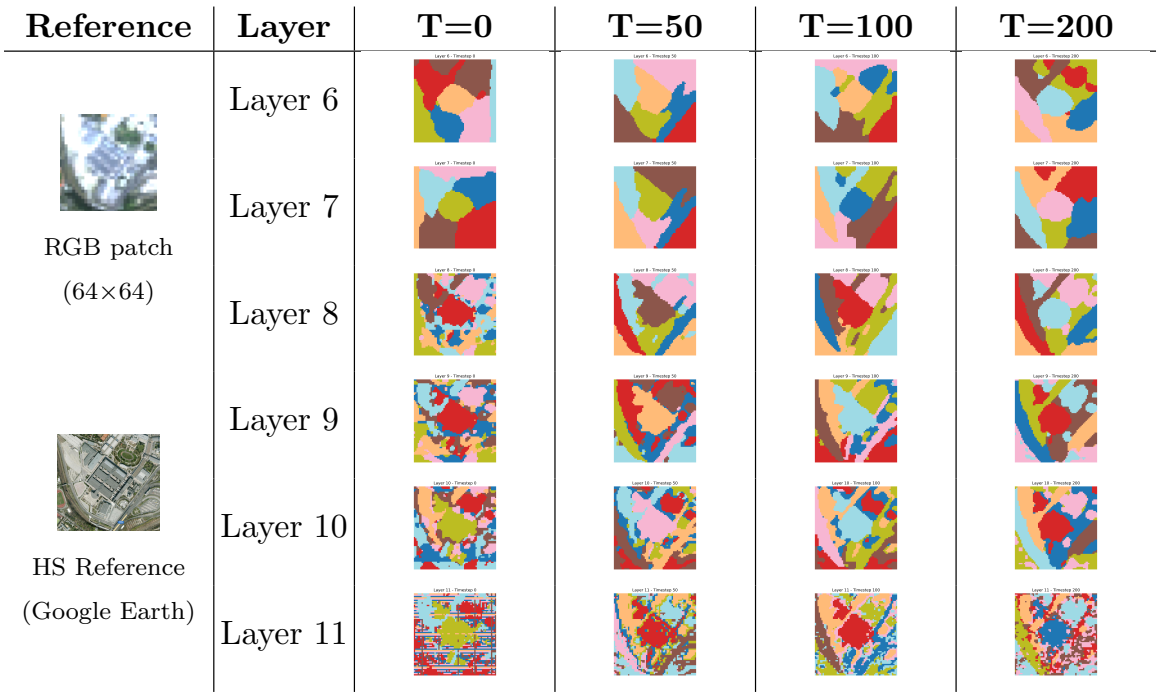

Figure 5: **Feature clustering across decoder layers and timesteps.** K-means clustering (k=6) is applied to decoder features from layers 6–11 across timesteps T=0 to T=200. The input is a 64×64 pseudo-RGB patch from Berlin HSI. Left: original pseudo-RGB patch and a Google Earth reference are shown for context. Cluster colors are not consistent across images.

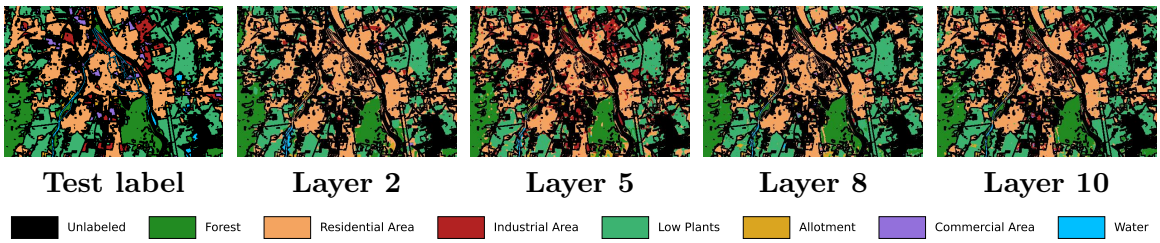

Figure 6: Visualization of the test label and informative layers (Layer 2, Layer 5, Layer 8, Layer 10) from GeoDiffNet with a fixed timestep of 50 for the Augsburg dataset. Higher layers capture more detailed and accurate features.

Table 5: Performance across U-Net decoder layers using spatial features at **timestep 0** on the **Augsburg** dataset.

	Layer											
	1	2	3	4	5	6	7	8	9	10	11	12
Forest	78.29	83.17	80.12	83.47	80.52	89.14	83.23	90.49	91.62	92.78	92.70	91.98
Residential	95.36	96.69	97.16	98.49	89.51	98.39	98.92	98.59	98.25	98.04	98.12	91.00
Industrial	14.78	15.46	16.89	18.33	79.06	25.64	12.53	15.74	35.69	61.46	46.06	73.13
Low Plants	73.70	79.94	86.42	83.54	74.97	86.72	91.01	91.12	93.80	95.98	93.25	91.52
Allotment	28.30	26.00	29.45	36.71	57.17	57.17	47.23	70.36	75.72	86.42	78.97	55.64
Commercial	1.71	2.08	1.28	0.98	0.98	4.21	2.93	8.30	8.85	6.35	4.27	3.60
Water	10.35	10.22	11.15	16.39	11.41	16.39	15.66	17.85	18.91	14.33	14.80	13.07
OA (%)	76.92	80.44	82.42	82.74	78.85	85.34	85.24	86.87	88.91	90.98	89.21	86.86
AA (%)	43.21	44.79	46.07	48.27	56.23	53.95	50.22	56.06	60.41	65.05	61.17	59.99
Kappa	0.6552	0.7096	0.7381	0.7434	0.7023	0.7836	0.7792	0.8059	0.8368	0.8682	0.8424	0.8125

Table 6: Performance across U-Net decoder layers using spatial features at **timestep 50** on the **Augsburg** dataset.

	Layer											
	1	2	3	4	5	6	7	8	9	10	11	12
Forest	72.01	71.51	79.22	78.01	81.18	68.75	86.63	91.53	90.40	90.88	89.84	89.41
Residential	91.73	94.53	95.77	95.42	96.27	95.99	97.79	97.36	97.00	97.16	92.93	97.44
Industrial	6.76	4.23	12.09	5.27	10.23	7.18	9.95	16.53	26.34	25.56	49.19	31.70
Low Plants	58.86	67.56	70.32	74.74	74.21	79.45	77.61	78.42	82.91	81.85	76.92	75.49
Allotment	10.71	6.50	13.96	21.99	26.58	23.90	18.16	24.67	30.40	39.77	46.08	24.47
Commercial	0.12	0.00	0.73	0.98	0.92	1.04	0.73	3.17	4.27	4.33	4.40	2.56
Water	4.58	10.29	9.29	13.87	15.20	9.22	16.99	12.08	14.73	14.47	9.36	10.22
OA (%)	68.68	72.62	75.81	76.79	77.79	77.05	80.44	81.72	83.53	83.33	80.93	81.08
AA (%)	34.97	36.37	40.20	41.47	43.51	40.79	43.98	46.25	49.44	50.58	52.67	47.33
Kappa	0.526	0.585	0.639	0.651	0.667	0.653	0.708	0.730	0.757	0.755	0.727	0.723

Table 7: Performance across U-Net decoder layers using spatial features at **timestep 100** on the **Augsburg** dataset.

	Layer											
	1	2	3	4	5	6	7	8	9	10	11	12
Forest	68.48	72.04	81.40	66.32	80.56	87.77	91.22	91.39	92.15	88.45	90.21	83.80
Residential	94.22	92.78	94.63	90.25	94.20	93.99	79.94	95.45	94.78	96.05	94.90	94.77
Industrial	2.66	3.16	5.17	4.80	6.03	13.89	47.68	19.19	19.95	26.61	42.56	36.53
Low Plants	46.79	50.92	56.24	58.36	61.84	71.91	60.70	67.32	76.30	77.09	75.70	70.79
Allotment	8.80	5.93	3.63	19.69	19.31	21.41	20.08	25.24	26.58	26.96	22.18	23.71
Commercial	0.55	0.00	0.06	2.75	0.98	1.40	0.67	0.67	1.53	3.72	4.82	4.15
Water	1.66	4.11	8.10	6.04	6.50	12.08	11.75	12.21	10.82	11.94	11.15	9.82
OA (%)	64.63	66.14	70.47	67.00	72.21	77.35	70.28	77.24	80.23	80.75	80.90	77.73
AA (%)	31.88	32.71	35.61	35.46	38.49	43.21	44.58	44.50	46.01	47.26	48.79	46.22
Kappa	0.4600	0.4875	0.5578	0.5047	0.5830	0.6644	0.5823	0.6665	0.7085	0.7165	0.7211	0.6749

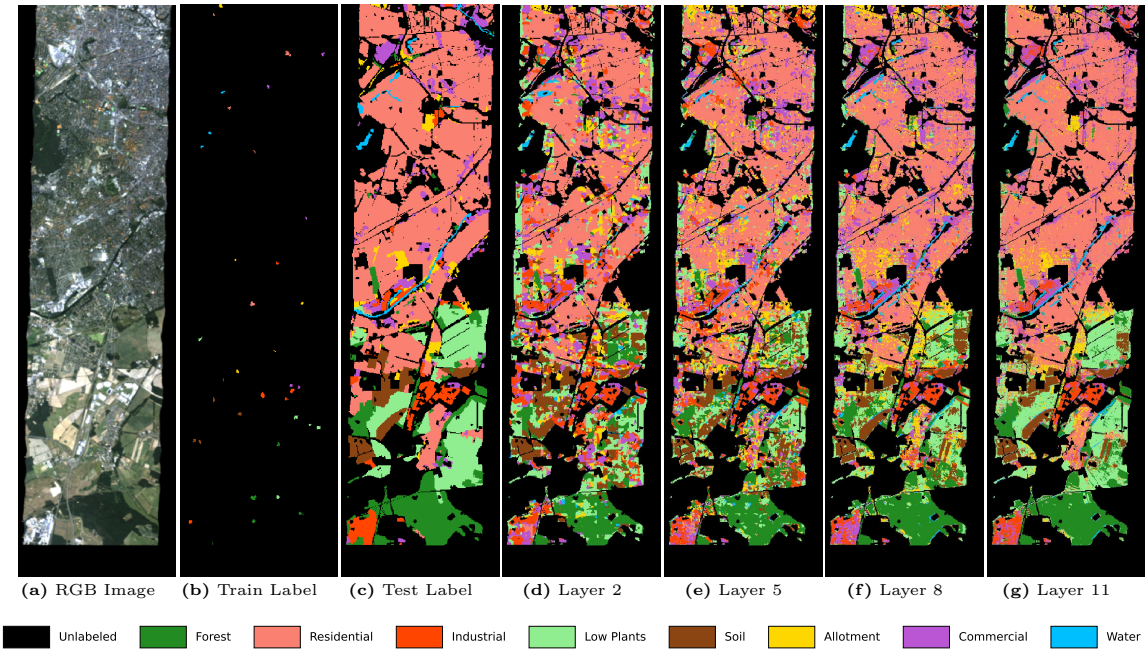

Figure 7: Visualization of informative layers from GeoDiffNet with a fixed timestep of 50 for the Berlin dataset. (a) RGB bands from HSI data, (b) training labels, (c) test labels for comparison. (d)–(g): Outputs from Layer 2, 5, 8, and 11 of GeoDiffNet, with Layer 11 yielding the clearest spatial features.

Table 8: Performance across U-Net decoder layers using spatial features at **timestep 0** on the **Berlin** dataset.

	Decoder Layer											
	1	2	3	4	5	6	7	8	9	10	11	12
Forest	38.56	52.75	64.47	55.10	58.41	65.10	66.25	69.62	64.92	68.34	63.12	62.90
Residential Area	59.11	53.90	50.57	64.03	62.27	68.87	66.76	57.65	64.44	66.86	60.65	43.53
Industrial Area	52.76	50.15	53.30	47.72	50.50	51.01	58.71	46.42	42.80	31.76	45.54	42.29
Low Plants	30.74	23.27	32.32	35.19	47.49	51.82	50.42	56.65	62.45	61.25	73.47	72.55
Soil	58.19	69.31	75.92	71.57	68.91	81.53	70.89	80.98	72.42	60.24	81.88	72.24
Allotment	23.13	36.28	43.72	33.67	46.69	43.95	46.32	55.62	54.58	43.20	59.08	63.15
Commercial Area	38.93	43.87	49.03	38.02	37.31	33.12	42.19	38.40	38.04	36.92	41.76	42.94
Water	26.87	30.02	36.43	38.45	48.28	57.97	46.74	55.28	44.05	33.51	65.24	56.75
OA (%)	50.23	48.91	50.46	56.30	57.73	63.22	62.27	58.22	61.68	61.89	61.76	51.24
AA (%)	41.04	44.94	50.72	47.97	52.48	56.67	56.03	57.58	55.46	50.26	61.34	57.05
Kappa	0.3246	0.3275	0.3584	0.3964	0.4218	0.4813	0.4735	0.4405	0.4684	0.4604	0.4807	0.3854
Mean IoU	0.2275	0.2372	0.2659	0.2786	0.3097	0.3434	0.3469	0.3413	0.3412	0.3227	0.3669	0.3203
Mean F1 Score	0.3493	0.3642	0.4002	0.4126	0.4515	0.4855	0.4906	0.4838	0.4815	0.4555	0.5090	0.4619

Table 9: Performance across U-Net decoder layers using spatial features at **timestep 0** on the **Berlin** dataset.

Table 10: Performance across U-Net decoder layers using spatial features at **timestep 50** on the **Berlin** dataset.

	Decoder Layer											
	1	2	3	4	5	6	7	8	9	10	11	12
Forest	41.61	46.89	51.29	57.51	55.62	67.41	63.74	68.91	62.08	70.53	**75.35**	72.16
Residential	64.12	59.10	61.82	51.17	60.95	68.47	63.88	63.92	63.06	68.57	**77.82**	52.94
Industrial	46.45	51.75	50.74	36.78	43.42	47.00	46.77	43.74	24.27	40.98	**53.41**	47.86
Low Plants	22.13	31.78	26.54	31.97	37.30	39.35	35.64	46.82	61.76	53.11	**71.50**	62.40
Soil	52.64	71.20	68.97	70.70	67.28	70.45	73.14	74.44	61.76	79.67	**75.12**	65.28
Allotment	25.63	23.17	18.35	21.66	27.56	33.00	45.34	34.60	32.56	47.99	**36.86**	48.98
Commercial	25.30	33.70	32.83	45.36	31.65	39.32	45.81	46.20	61.74	45.94	**40.41**	64.45
Water	8.67	17.04	14.24	33.80	29.11	41.14	50.29	53.18	50.09	50.58	**54.74**	47.02
OA (%)	51.02	51.37	52.45	48.21	53.87	60.89	58.23	59.97	60.02	64.06	**72.15**	57.08
AA (%)	35.82	41.83	40.60	43.62	44.11	50.77	53.08	53.98	52.17	57.17	**60.65**	57.63
Kappa	0.3072	0.3358	0.3443	0.3228	0.3662	0.4438	0.4241	0.4462	0.4495	0.4917	**0.5850**	0.4360
Mean IoU	0.2054	0.2294	0.2331	0.2375	0.2522	0.3126	0.3102	0.3270	0.3341	0.3586	**0.4218**	0.3634
Mean F1 Score	0.3151	0.3509	0.3497	0.3632	0.3783	0.4487	0.4504	0.4677	0.4708	0.5025	**0.5629**	0.5077

Table 11: Performance across U-Net decoder layers using spatial features at **timestep 100** on the **Berlin** dataset.

	Decoder Layer											
	1	2	3	4	5	6	7	8	9	10	11	12
Forest	34.93	43.26	44.97	52.28	52.38	57.18	59.66	57.65	58.18	**66.15**	62.33	55.82
Residential	54.48	55.39	57.23	57.96	57.43	**63.49**	53.49	59.29	60.49	60.29	52.80	46.99
Industrial	42.27	32.49	28.64	18.05	30.75	37.95	**38.93**	41.17	36.93	39.07	40.88	40.72
Low Plants	18.32	19.48	17.04	24.92	25.01	29.01	28.15	42.90	46.14	46.99	57.17	**61.16**
Soil	56.90	44.43	66.18	65.56	74.41	75.75	**79.67**	73.89	74.60	**81.11**	75.01	74.26
Allotment	16.05	18.63	19.60	18.60	14.51	16.43	37.44	37.69	42.66	38.87	**64.45**	51.58
Commercial	26.39	36.43	44.55	47.10	49.73	51.25	53.76	55.04	52.16	51.43	47.82	**65.08**
Water	5.40	10.72	7.37	22.15	31.01	25.90	36.51	45.63	46.82	43.76	45.32	**52.55**
OA (%)	43.88	45.36	47.37	49.52	50.23	55.24	50.68	55.77	56.80	**57.87**	54.77	51.76
AA (%)	31.84	32.60	35.70	38.33	41.90	44.62	48.45	51.66	52.25	53.46	55.72	**56.02**
Kappa	0.2368	0.2631	0.2820	0.3088	0.3210	0.3748	0.3496	0.3994	0.4106	**0.4260**	0.4092	0.3835
Mean IoU	0.1683	0.1831	0.2005	0.2126	0.2357	0.2605	0.2611	0.3080	0.3174	**0.3209**	0.3434	0.3137
Mean F1 Score	0.2662	0.2860	0.3086	0.3272	0.3576	0.3851	0.3929	0.4490	0.4581	**0.4609**	0.4897	0.4584

B.2. Berlin Dataset

B.2.1. Visualization

Using the same method, we test on the Berlin dataset with a fixed timestep of 50 and evaluate layer informativeness based on performance. As shown in Figure 7, it presents the different layers (Layers 2, 5, 8, and 11) from the GeoDiffNet model for the Berlin dataset, comparing with the test label. higher layers provide more detailed and accurate feature representations. Specifically, higher layers (Layer 11) demonstrate more refined and precise feature delineations and improved classification accuracy compared to the lower layers.

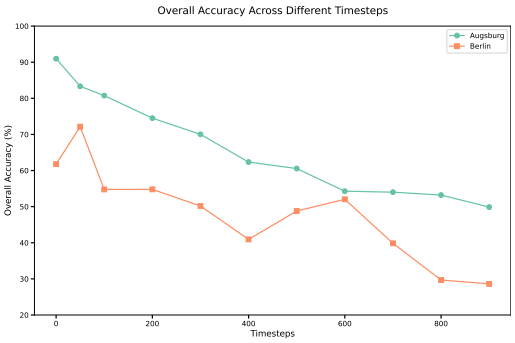

Figure 8: **Overall accuracy across diffusion timesteps** t for the Augsburg and Berlin datasets. Accuracy is highest when features are extracted at early timesteps, indicating stronger transferability. Optimal performance occurs at t=0 for Augsburg and t=50 for Berlin.

B.2.2. Peformance over layer at timestep 0, 50, 100

Quantitatively, as shown in Table 9, Table 10, and Table 11 , we conducted the same experiment for the Berlin dataset, analyzing different layers across timesteps 0, 50, and 100. The results demonstrate a consistent trend: both overall and per-class performance metrics improve with increasing layer depth, peaking around Layer 11.

Appendix C. The Impact of Time Steps(noise)

C.1. Initial timesteps has more transferbilty

$t = 0$, we extract the feature representation of the clean image x_0. As t increases, more noise is added, transforming the image to x_t. In this ablation study, we investigate the impact of different timesteps on feature extraction in diffusion models.

There are varying perspectives on the optimal timestep selection, largely depending on the dataset. According to Xu et al. (2023), clean images, devoid of noise, extract the most optimal features. Conversely, Luo et al. (2023) posits that the choice of timestep acts as a control mechanism, determining the level of high-frequency detail retained in the images. This selection helps to implicitly map noisy inputs to smoother outputs, thereby enhancing classification accuracy and overall model performance.

Zhong et al. (2024), in their *Chain of Forgetting theorem*, elucidates how a diffusion model manages the denoising (generation) process over time. As $t \to 0$, the model zeroes in on the closest sample in the training dataset, executing a general denoising process with higher transferability. However, as $t \to T$, the model's output aligns with the mean of the training data distribution, necessitating domain adaptation.

Although the Chain of Forgetting theorem primarily addresses the generation process, Luo et al. (2023) observes that inversion (forward) processes contain information analogous to the generation process at the same timestep. Based on their insights, we infer that during the forward (inversion) process of feature extraction, initial stages exhibit higher transferability, although the exact optimal timestep remains uncertain.

Table 12: Performance metrics for GeoDiffNet at different **timesteps (0–900)** using **Layer 11** for spatial features extracted from the **Augsburg** dataset.

Class	Timesteps										
	TS 0	TS 50	TS 100	TS 200	TS 300	TS 400	TS 500	TS 600	TS 700	TS 800	TS 900
Forest	92.78	90.88	88.45	88.35	86.03	79.46	78.62	68.71	76.38	69.34	58.06
Residential	98.04	97.16	96.05	91.66	89.92	71.60	82.82	81.19	68.07	64.68	80.77
Industrial	61.46	25.56	26.61	14.70	10.68	5.85	7.08	8.02	1.15	0.99	1.20
Low Plants	95.98	81.85	77.09	66.20	57.05	59.72	42.10	29.75	41.82	46.89	24.66
Allotment	86.42	39.77	26.96	14.53	4.97	5.54	2.29	6.12	0.76	0.96	0.00
Commercial	6.35	4.33	3.72	3.36	3.48	0.73	1.65	0.49	0.24	0.00	0.12
Water	14.33	14.47	11.94	6.44	6.17	2.46	1.99	15.13	1.59	1.46	1.33
Overall Accuracy (%)	90.98	83.33	80.75	74.51	70.03	62.35	60.55	54.28	54.01	53.21	49.88
AA (%)	65.05	50.58	47.26	40.75	36.90	32.20	30.94	29.92	27.15	26.33	23.73
Kappa Coefficient	0.8682	0.7549	0.7165	0.6216	0.5542	0.4414	0.4116	0.3359	0.3166	0.3037	0.2398
Mean IoU	0.5482	0.4124	0.3857	0.3285	0.2883	0.2396	0.2290	0.2028	0.1912	0.1854	0.1584
Mean F1 Score	0.6400	0.5092	0.4813	0.4228	0.3756	0.3211	0.3088	0.2869	0.2637	0.3023	0.2669

Table 13: Performance metrics for GeoDiffNet at different **timesteps (0–900)** using **Layer 10** for spatial features extracted from the **Berlin** dataset.

Class	Timesteps										
	TS 0	TS 50	TS 100	TS 200	TS 300	TS 400	TS 500	TS 600	TS 700	TS 800	TS 900
Forest	63.12	75.35	62.33	63.86	62.45	65.33	48.14	45.50	27.81	35.20	28.52
Residential	60.65	77.82	52.80	53.92	50.82	36.84	51.86	63.90	48.55	31.63	32.98
Industrial	45.54	53.41	40.88	34.64	50.94	49.57	59.36	64.58	50.61	33.82	18.55
Low Plants	73.47	71.50	57.17	59.39	45.71	29.62	47.40	23.84	16.94	16.56	18.83
Soil	81.88	75.12	75.01	70.45	64.22	74.76	74.21	81.00	68.87	59.61	39.60
Allotment	59.08	36.86	64.45	44.97	32.78	35.62	14.20	5.87	14.87	21.50	9.98
Commercial	41.76	40.41	47.82	41.67	31.89	35.39	22.76	10.98	19.53	14.51	21.11
Water	65.24	54.74	45.32	59.54	26.51	25.52	9.70	6.60	8.17	5.35	4.14
Overall Accuracy (%)	61.76	72.15	54.77	54.79	50.18	40.94	48.79	52.03	39.85	29.69	28.62
AA (%)	61.34	60.65	55.72	53.56	45.66	44.08	40.95	37.78	31.92	27.27	21.71
Kappa Coefficient	0.4807	0.5850	0.4092	0.4009	0.3428	0.2689	0.3032	0.2960	0.1863	0.1234	0.0912
Mean IoU	0.3669	0.4218	0.3434	0.3274	0.2930	0.2450	0.2331	0.2078	0.1595	0.1252	0.1028
Mean F1 Score	0.5090	0.5629	0.4897	0.4694	0.4254	0.3228	0.3547	0.3143	0.2573	0.2110	0.1772

C.2. Experiment amd results

We conducted experiments at initial timesteps (0, 50, 100) and continued with increments of 100 timesteps, with a fixed best layer: Layer 10 for the Augsburg dataset and Layer 11 for the Berlin dataset. Our objective was to evaluate the transferability of features extracted during the forward (inversion) process with different timesteps. The evaluation result can be seen from Table 12 and Table 13. From Figure 8, we can see that the best timesteps differ, with optimal performance observed at timestep 0 for Augsburg and timestep 50 for Berlin. However, the common observation is that performance decreases after the initial stages as noise increases, which matches our initial inference.

Appendix D. Pre-trained Diffusion Model Architecture

The pre-trained model uses OpenAI's pre-trained 64×64 diffusion model Dhariwal and Nichol (2021), which can find its detailed information and be downloaded from the following repository:

https://github.com/openai/guided-diffusion?tab=readme-ov-file.

Table 14: Decoder architecture: resolution, channels, and attention usage.

Layer	Resolution	Channels	Attn.
1	8×8	768	✓
2	8×8	768	✓
3	16×16	768	✓
4	16×16	576	✓
5	16×16	576	✓
6	16×16	576	✓
7	32×32	576	✓
8	32×32	384	✓
9	32×32	384	✓
10	32×32	384	✓
11	64×64	384	
12	64×64	192	

In the context of geospatial images, the 64×64 patch size provide extensive spatial context compared to conventional 11×11 patches used in fully-supervised HSI methods. Unlike traditional approaches that are constrained to small patches due to overfitting and training stability issues with limited supervision, our pre-trained diffusion backbone enables effective utilization of larger spatial contexts without data efficiency limitations.

Table 14 lists the pre-trained model's decoder activation dimensions at different layers. Layers are numbered from bottom to top, including feature map resolution and channel dimension which facilitate extracting diffusion features at each layer. The design choices (i.e., the resolution and the number of channels) were determined experimentally.